Constraints on TESS albedos for five hot Jupiters

Martin Blažek, Petr Kabáth, Anjali A. A. Piette, Nikku Madhusudhan, Marek Skarka, Ján Šubjak, David R. Anderson, Henri M. J. Boffin, Claudio C. Cáceres, Neale P. Gibson, et al.

Monthly Notices of the ROYAL ASTRONOMICAL SOCIETY

MNRAS **513,** 3444–3457 (2022)
Advance Access publication 2022 April 9

https://doi.org/10.1093/mnras/stac992

Constraints on *TESS* albedos for five hot Jupiters

Martin Blažek [1,2]★ Petr Kabáth [1] Anjali A. A. Piette [3,4] Nikku Madhusudhan [3] Marek Skarka [1,2] Ján Šubjak,[1,5] David R. Anderson [6] Henri M. J. Boffin [7] Claudio C. Cáceres [8,9] Neale P. Gibson [10] Sergio Hoyer [11] Valentin D. Ivanov[7,12] and Patricio M. Rojo[13]

[1]*Astronomical Institute of the Czech Academy of Sciences, Fričova 298, 251 65 Ondřejov, Czech Republic*
[2]*Department of Theoretical Physics and Astrophysics, Faculty of Science, Masaryk University, Kotlářská 267/2, 611 37 Brno, Czech Republic*
[3]*Institute of Astronomy, University of Cambridge, Madingley Road, Cambridge CB3 0HA, UK*
[4]*Earth and Planets Laboratory, Carnegie Institution for Science, 5241 Broad Branch Road, NW, Washington, DC 20015, USA*
[5]*Astronomical Institute of Charles University, V Holešovičkách 2, 180 00, Praha, Czech Republic*
[6]*Astrophysics Group, Keele University, Staffordshire ST5 5BG, UK*
[7]*European Southern Observatory, Karl-Schwarzschild-Str. 2, D-85748 Garching bei München, Germany*
[8]*Departamento de Ciencias Físicas, Facultad de Ciencias Exactas, Universidad Andrés Bello, Av. Fernandez Concha 700, Las Condes, Santiago, Chile*
[9]*Núcleo Milenio de Formación Planetaria – NPF, Av. Gran Bretaña 1111, Valparaíso, Chile*
[10]*School of Physics, Trinity College Dublin, The University of Dublin, Dublin 2, Ireland*
[11]*Aix Marseille Université, CNRS, CNES, Laboratoire d'Astrophysique de Marseille UMR 7326, F-13388, Marseille, France*
[12]*European Southern Observatory, Ave. Alonso de Córdova 3107, Vitacura, Santiago, Chile*
[13]*Departamento de Astronomía, Universidad de Chile, Camino El Observatorio 1515, Las Condes, Santiago, Chile*

Accepted 2022 April 5. Received 2022 April 5; in original form 2022 February 6

ABSTRACT

Photometric observations of occultations of transiting exoplanets can place important constraints on the thermal emission and albedos of their atmospheres. We analyse photometric measurements and derive geometric albedo (A_g) constraints for five hot Jupiters observed with *TESS* in the optical: WASP-18 b, WASP-36 b, WASP-43 b, WASP-50 b, and WASP-51 b. For WASP-43 b, our results are complemented by a VLT/HAWK-I observation in the near-infrared at 2.09 μm. We derive the first geometric albedo constraints for WASP-50 b and WASP-51 b: $A_g < 0.445$ and $A_g < 0.368$, respectively. We find that WASP-43 b and WASP-18 b are both consistent with low geometric albedos ($A_g < 0.16$) even though they lie at opposite ends of the hot Jupiter temperature range with equilibrium temperatures of ∼1400 K and ∼2500 K, respectively. We report self-consistent atmospheric models that explain broad-band observations for both planets from *TESS*, *HST*, *Spitzer*, and VLT/HAWK-I. We find that the data of both hot Jupiters can be explained by thermal emission alone and inefficient day–night energy redistribution. The data do not require optical scattering from clouds/hazes, consistent with the low geometric albedos observed.

Key words: techniques: photometric – planets and satellites: atmospheres – stars: individual: WASP targets – infrared: planetary systems – methods: data analysis.

1 INTRODUCTION

Thermal emission observations of exoplanet atmospheres provide essential insights into their chemical compositions, thermal structures, energy transport, and clouds/hazes (e.g. Burrows, Ibgui & Hubeny 2008b; Cowan & Agol 2011; Parmentier et al. 2016; Madhusudhan 2019). In particular, optical and near-infrared occultation photometry allows the albedo (or reflectance) of an exoplanet to be measured (e.g. Cowan & Agol 2011; Angerhausen, DeLarme & Morse 2015; Esteves, De Mooij & Jayawardhana 2015; Mallonn et al. 2019). The albedo, in turn, provides key insights into the physical properties of the atmosphere, including the presence of clouds and hazes (e.g. Burrows et al. 2008b). To study exoplanetary atmospheres, two measures of albedo are typically used. While the Bond albedo measures the fraction of stellar light reflected over all wavelengths, the geometric albedo A_g is wavelength dependent. Specifically, the latter is used to describe the reflectance of an atmosphere at optical wavelengths.

A high albedo is indicative of significant optical scattering in the atmosphere and can therefore indicate the presence of clouds and/or hazes. To date, a range of albedo measurements have been made for exoplanetary atmospheres, suggesting clear to cloudy atmospheres. For example, several hot Jupiters have been found to have low albedos and are therefore thought to have little or no cloud coverage in the photosphere, e.g. TrES-2 b ($A_g = 0.025$, Kipping & Spiegel 2011), WASP-12 b ($A_g < 0.064$, Bell et al. 2017), and WASP-18 b ($A_g < 0.048$, Shporer et al. 2019). Meanwhile, several exoplanets across the mass range have been found to have larger albedos, suggesting more significant clouds and/or hazes, e.g. HD 189733 b ($A_g = 0.40 \pm 0.12$, Evans et al. 2013), Kepler-7 b ($A_g = 0.35 \pm 0.02$, Demory et al. 2011, 2013), HAT-P-11 b ($A_g = 0.39 \pm 0.07$, Huber, Czesla & Schmitt 2017), Kepler-10 b ($A_g < 0.61$, Batalha et al. 2011). Furthermore, phase-curve offsets observed in some exoplanets by the *Kepler* space

★ E-mail: deathlosopher@seznam.cz

telescope (Borucki et al. 2010; Demory et al. 2013; Angerhausen et al. 2015; Esteves et al. 2015; Shporer & Hu 2015) suggest that clouds may be more prevalent in cooler planets, with a transition at ∼1900 K between cloudy and non-cloudy atmospheres (Parmentier et al. 2016). Albedo measurements of hot Jupiters across a range of temperatures are therefore needed to further elucidate the presence of clouds and hazes across this regime.

Constraints on exoplanetary albedos also provide important information about the thermal properties of their atmospheres. Optical scattering from clouds and hazes cools the dayside, affecting the brightness temperatures measured in occultations (e.g. Morley et al. 2013). This can in turn affect inferences of day–night energy redistribution, as the cooling due to clouds/hazes may be degenerate with the effects of energy redistribution (Cowan & Agol 2011). Previous studies of hot Jupiters have revealed typically low albedos (Cowan & Agol 2011; Angerhausen et al. 2015; Esteves et al. 2015; Mallonn et al. 2019), and the Transiting Exoplanet Survey Satellite (*TESS*; Ricker et al. 2015) will provide valuable new constraints as it continues to expand the population of hot Jupiters with albedo measurements.

Near-infrared (NIR) and optical observations probe different atmospheric properties and are therefore highly complementary. In particular, the NIR probes thermal emission from exoplanet atmospheres and can place constraints on their chemical compositions and thermal profiles. The High Acuity Wide-field K-band Imager (HAWK-I) on the Very Large Telescope (VLT) probes the ∼0.9–2.4-μm range and is well-suited to probing such thermal emission (e.g. Anderson et al. 2010; Gibson et al. 2010). Meanwhile, *TESS* operates in the 0.6–1-μm range and is ideally suited to search for reflected light from exoplanet atmospheres (e.g. Shporer et al. 2019; Beatty et al. 2020). To date, *TESS* has made confirmed detections of over a hundred exoplanets, with more than a thousand detections currently awaiting confirmation. While its primary goal is to search for new exoplanets orbiting bright stars, many occultations of already known exoplanets have been detected with *TESS* phase curves (e.g. Shporer et al. 2019; Bourrier et al. 2020). The growing population of exoplanets with *TESS* data is allowing comprehensive studies of atmospheric albedos across a range of exoplanets (Wong et al. 2020a).

Our primary goal in this work is to constrain occultation depths, using observations from *TESS* in the optical and from HAWK-I in the near-infrared, of these hot Jupiters: WASP-18 b, WASP-36 b, WASP-43 b, WASP-50 b, and WASP-51 b. This in turn leads to constraints on the albedos of these planets, providing clues about their thermal properties, energy redistribution, and clouds. We further use *TESS* and HAWK-I data, in addition to existing *Spitzer* data, to investigate atmospheric models for two hot Jupiters at opposite ends of the temperature range: WASP-43 b (Hellier et al. 2011), with an equilibrium temperature of ∼1400 K, and WASP-18 b (Southworth et al. 2009), with an equilibrium temperature of ∼2500 K. In particular, WASP-18 b is at the transition between the *hot* and *ultra-hot* subcategories of hot Jupiters. This is an important regime as there can be significant changes in atmospheric properties, including the thermal dissociation of molecules (e.g. Arcangeli et al. 2018; Gandhi, Madhusudhan & Mandell 2020; Lothringer, Barman & Koskinen 2018; Parmentier et al. 2018) and the presence of thermal inversions (e.g. Baxter et al. 2020).

This article is structured as follows. In Section 2, we describe the data sets and instrumentation, in Section 3 we present data analysis, our results are presented in Section 4, and in Section 5 we discuss atmospheric properties of the studied exoplanets.

2 OBSERVATIONS

We investigate occultation observations of hot Jupiters with two different facilities: *TESS* in the optical from space and VLT HAWK-I in the near-infrared on the ground. The observations include data sets of five occultations observed with *TESS* and one occultation observed with HAWK-I. In what follows, we describe these observations.

2.1 Target selection

We selected WASP targets for our study which were discovered in a scope of the WASP survey (Pollacco et al. 2006). They include the following exoplanetary systems: WASP-18 (Hellier et al. 2009), WASP-36 (Smith et al. 2012b), WASP-43 (Hellier et al. 2011), WASP-50 (Gillon et al. 2011), and WASP-51 (Johnson et al. 2011).

The chosen targets were originally selected from unpublished (all but one) HAWK-I data in the ESO Science Archive. Usually, these targets were observed because of the expected larger, and thus favourable, occultation depth. We investigate if by using modern techniques such as Gaussian process-based methods, we could extract meaningful science from these neglected data, and to draw – if possible – some conclusion for future occultation observations. Due to the insufficient quality of the HAWK-I data to detect an occultation or to put meaningful upper limits, we further describe in this work only one HAWK-I archival data set – WASP-43. The data are based on an observation made with ESO Telescope at the La Silla Paranal Observatory under programme ID 086.C-0222 (PI Michaël Gillon). The data set was used as a test benchmark for which occultation was published by Gillon et al. (2012) and we re-analysed it with a different method.

Next, we mined the *TESS* archive for observations of our original HAWK-I objects, and found that they all have been monitored between 2018 and 2021 in various *TESS* sectors, so we used all the available data for this work.

The orbital and physical properties of all studied exoplanetary systems are listed in Table 1.

2.2 Instruments used to acquire the data sets

The Transiting Exoplanet Survey Satellite (Ricker et al. 2015) contains four wide-angle 10-cm telescopes with associated CCDs working in the wavelength bandpass between 600 and 1000 nm centred on 786.5 nm. As *TESS* observes brighter stars, the brightness of our targets is between 8.8 and 12.2 mag in the optical *TESS* band. Since the start of its operation in 2018, *TESS* has been photometrically observing almost the whole sky in sectors, each covering a field of view 24° × 96°.

The instrument used to get the ground-based data described in this article is the High Acuity Wide-field *K*-band Imager (HAWK-I) at Very Large Telescope of ESO (Pirard et al. 2004; Casali et al. 2006; Kissler-Patig et al. 2008; Siebenmorgen et al. 2011). It hosts six narrow-band filters and the field of view of HAWK-I is 7.5 arcmin × 7.5 arcmin. The detector is composed of four chips, each of them with 2048 × 2048 px and works in the near-infrared band between 0.85 and 2.50 μm. The pixel scale of HAWK-I is 0.1064 arcsec px^{-1}. For more details, see HAWK-I User Manual.[1]

[1] https://www.eso.org/sci/facilities/paranal/instruments/hawki/doc.html

Table 1. Stellar characteristics and physical properties of the planetary systems analysed in this article.

System	RA (α)	Dec. (δ)	Type	$T_{\mathrm{eff},\star}$ (K)	m_{TESS} (mag)	R_{p} (R_{J})	M_{p} (M_{J})	a (au)	P (d)
WASP-18[a]	$01^{\mathrm{h}}37^{\mathrm{m}}25^{\mathrm{s}}$	$-45^{\circ}40'40''$	F6V	6431	8.83	1.165	10.43	0.021	0.94
WASP-36[b]	$08^{\mathrm{h}}46^{\mathrm{m}}20^{\mathrm{s}}$	$-08^{\circ}01'37''$	G2	5900	12.15	1.281	2.303	0.026	1.54
WASP-43[c]	$10^{\mathrm{h}}19^{\mathrm{m}}38^{\mathrm{s}}$	$-09^{\circ}48'23''$	K7V	4520	11.02	1.036	2.034	0.015	0.81
WASP-50[d]	$02^{\mathrm{h}}54^{\mathrm{m}}45^{\mathrm{s}}$	$-10^{\circ}53'53''$	G9V	5400	11.01	1.138	1.437	0.029	1.96
WASP-51[e]	$08^{\mathrm{h}}15^{\mathrm{m}}48^{\mathrm{s}}$	$+05^{\circ}50'12''$	G0	6250	9.91	1.420	0.760	0.042	2.81

Note. RA is the right ascension, Dec. is the declination, $T_{\mathrm{eff},\star}$ is the effective temperature of the star, m_{TESS} is the apparent magnitude in the *TESS* bandpass, R_{p} and M_{p} are the stellar radius and the mass, respectively, a is the semimajor axis of the orbit, and P is the orbital period of the planet. WASP-51 corresponds to HAT-P-30. [a]Southworth et al. (2009), [b]Smith et al. (2012b), [c]Gillon et al. (2012), [d]Tregloan-Reed & Southworth (2013), and [e]Enoch et al. (2011).

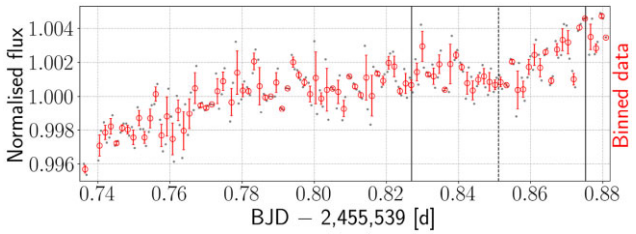

Figure 1. The raw light curve of WASP-43 system (HAWK-I, NB2090). The normalized raw light curve showing all data (the grey points) and data binned per 2 min (the red circles with error bars) is depicted. The vertical lines show the calculated beginning, the centre, and the end of the occultation.

2.3 Observations and data reduction

While *TESS* data are primarily intended to detect new exoplanets, here they serve as a probe of potential reflected light in the optical wavelength range. The HAWK-I data set analysed here is the result of an observing run proposed to study atmospheres of highly irradiated transiting exoplanets. For the data reduction and to perform aperture photometry of this data set we used the Image Reduction and Analysis Facility (IRAF; Tody, D. 1986, 1993). While data reduction includes removing of effects of the used instrument which are added to raw images by the detector, aperture photometry includes summing the light of a given star in an aperture and subtracting sky background.

2.3.1 TESS *full-phase data sets*

The available *TESS* data of our targets were obtained in 2-min cadence. The data sets analysed in this article were taken between 2018 August and 2021 March, each of the sets comprises between roughly 13 000 and 18 000 data points and covers between 9 and 27 orbital phases (depending on the orbital period). The targets were observed in *TESS* sectors 2–4, 7–9, 29–31, and 34–35.

To analyse the data, we used the Pre-search Data Conditioned Simple Aperture Photometry Flux, abbreviated as PDCSAP_FLUX (Smith et al. 2012a; Stumpe et al. 2012; Jenkins et al. 2016), which is the flux corrected for instrumental variations.

2.3.2 HAWK-I occultation data set

Our HAWK-I data set was downloaded from the ESO archive. This data were obtained through a narrow-band filter of HAWK-I – NB2090 (2.09 μm with width of 20 nm). This data set of WASP-43 has already been previously analysed and published (Gillon et al. 2012), using a Markov chain Monte Carlo algorithm (Gillon et al. 2010) to model the light curve. We selected this system as a benchmark for comparison of different fitting methods and for our re-analysis we used the Gaussian Processes method described in Gibson et al. (2012).

The data set was obtained in 2010 and consists of 184 science frames with integration time of 1.7 s. Three comparison stars were observed along with the target star. Standard photometric data reduction using flat-field frames was performed. Then differential aperture photometry was performed and the star with the most stable flux (TYC 5490-153-1) was used as a comparison star for the differential photometry. The obtained data points were then binned per 2 min time intervals.

During the observation, changes of meteorological conditions were as follows: humidity in a range 10–18 per cent, seeing in a range of 0.47–1.39 arcsec, and airmass decreasing from 2.10 to 1.05 as the star on the sky was rising during the whole observation.

The obtained light curve with the original data and the binned data is shown in Fig. 1.

3 ANALYSIS OF THE PHOTOMETRIC LIGHT CURVES

In this section, we describe the fitting methods used for all our data sets to derive occultation depths. We also present here the basic equations to theoretically estimate the occultation depth both from the reflected light and from thermal emission.

3.1 The fitting routines and detrending

To fit the data sets, we used two different software packages. For fitting the *TESS* phase curves, we used ALLESFITTER package and for fitting the HAWK-I data set we used GEEPEA modelling routine. These two methods are described in the following subsections.

3.1.1 'ALLESFITTER' software package

To fit the *TESS* phase curves, shown in Fig. 4, we used PYTHON-based ALLESFITTER software package (Günther & Daylan 2019, 2021). It was developed to model photometric and radial velocity data. To make systematic noise models, Gaussian processes (GP) are included. After running the code an initial guess is obtained, then inference via MCMC or Nested Sampling is initiated. The methods include tests to assess convergence and also residual diagnostics to check possible structure in residuals. For details about ALLESFITTER modelling package, see Günther & Daylan (2019, 2021) and the official website.[2]

[2]https://www.allesfitter.com/

We fitted and sampled from the posterior of the ratio of the planetary to the stellar radius $R_p/R_\star$, the sum of those radii divided by the semimajor axis $(R_p + R_\star)/a$, cosine of the inclination angle of the planetary orbit $\cos i$, epoch, i.e. the time of the centre of the transit T_0, the ratio of the surface brightness of the planet to the star J, logarithm of the error scaling of white noise used for the GP $\ln\sigma$, a baseline offset ΔF, the semiamplitude of the Doppler-boosting $A_{\rm beaming}$, the amplitude of the atmospheric contribution (both thermal and reflected) to the phase curve modulation $A_{\rm atmospheric}$, and the amplitude of the ellipsoidal modulation caused by tidal interaction between the host star and the planet $A_{\rm ellipsoidal}$. We fixed the orbital period of the planet P, eccentricity and argument of periastron (planetary orbit) $\sqrt{e}\cos\omega$ and $\sqrt{e}\sin\omega$, and limb darkening coefficients q_1 and q_2. The values of P, e, and ω were adopted from discovery articles of the particular exoplanetary systems (Table 1). To derive limb darkening coefficients we used the quadratic model of PYLDTK software package (Parviainen & Aigrain 2015 describing the package and Husser et al. 2013 describing the spectrum library).

The derived parameters from our fits were the host star radius divided by the semimajor axis $R_\star/a$, the semimajor axis divided by the host star radius $a/R_\star$, the planetary radius divided by the semimajor axis R_p/a, the planetary radius R_p, the semimajor axis of the planetary orbit a, the inclination angle of the planetary orbit i, the transit and occultation impact parameter $b_{\rm tra}$ and $b_{\rm occ}$, the total and full-transit duration $T_{\rm tot}$ and $T_{\rm full}$, the epoch of the occultation $T_{0;\,\rm occ}$, the equilibrium temperature of the planet $T_{\rm eq;\,p}$, the transit and occultation depth $\delta_{\rm tra}$ and $\delta_{\rm occ}$, the nightside flux of the planet $F_{\rm nightside;\,p}$, and host star density $\rho_\star$. Formulae of all derived parameters by ALLESFITTER are listed in table A3 of Günther & Daylan (2021).

We used all the *TESS* photometric data of the systems available to date. Particularly, for WASP-18 modelling, we used data of sectors 2, 3, 29, and 30, for WASP-36 data of sectors 8 and 34, for WASP-43 data of sectors 9 and 35, for WASP-50 data of sectors 4 and 31, and for WASP-51 data of sectors 7 and 34. For each sector of every system, we period-folded the light curves and then merged all the light curves of each system together. Finally, we binned the data sets per 5-min time intervals.

For each modelling, we used both MCMC and Nested Sampling method to fit our data and to derive parameters and their uncertainties. Both the methods perfectly agreed and gave results with negligible differences. As Nested Sampling ensures that all convergence criteria are fulfilled, we present only the results obtained from this method (Section 4.1).

3.1.2 'GEEPEA' routine

For fitting our HAWK-I data set (WASP-43), we used a Gaussian Processes method. The method is defined as an infinite set of Gaussian variables which have common Gaussian distribution. The systematics are modelled here as a stochastic process. The GP model, our eclipse model, is a set of a deterministic component and a stochastic component. These are represented here as a mean function (the light-curve model) and a kernel function (the noise model), respectively. To implement our GP, we used the GEEPEA code[3] as described in Gibson et al. (2013a, b) and Gibson (2014).

If we model a light curve of transit or occultation by using the GP, we have to assign parameters to the mean and kernel function (we will refer the parameters of the kernel function to 'hyperparameters'). The kernel function takes at least three hyperparameters: height scale ξ physically representing the typical range of the data points on the y-axis, a vector of length scale parameters $\boldsymbol{\eta}$ physically representing changes on the x-axis (distance between 'bumps'), and white noise σ_w^2. We assign an array of parameters to the mean function, which represents the light-curve model. These parameters are time of the occultation centre T_0, orbital period P, scaled semimajor axis $a/R_\star$, planet-star radii ratio $R_p/R_\star$, impact parameter b, out-of-transit flux $f_{\rm oot}$, time gradient $T_{\rm grad}$, expected occultation depth $\delta_{\rm occ}$ and, in the case of a primary transit, also limb darkening coefficients q_1 and q_2. As the HAWK-I data are obtained only during the planetary occultation, we fitted only the occultation.

Before the run of the fitting routine, P, $a/R_\star$, $R_p/R_\star$, and b were taken from literature and thus fixed. The fitted parameters were T_0, $f_{\rm oot}$, $T_{\rm grad}$, $\delta_{\rm occ}$, and hyperparameters of the kernel function ξ, $\boldsymbol{\eta}$, and σ_w^2. In our case, besides time (η_t), we used airmass (η_a) as the second component of the length scale vector $\boldsymbol{\eta}$.

To detrend the fitted light curve, we used polynomial regression of degree two assuming the out-of-occultation model to be a quadratic function of time $[f(t) = at^2 + bt + c]$. For the polynomial regression, we excluded data during the occultation. After inferring their values, we calculated the function $f(t)$ for all the data points. To get the detrended and normalized-to-one flux and the occultation model, we subsequently divided our data by the polynomial function.

We describe results of the HAWK-I light-curve fit of WASP-43 in Section 4.2.

3.2 Occultation depth estimation

One of the input parameters of the GEEPEA routine is an estimated flux drop during the occultation searched in our data which is then refined by the routine. The value is also needed to interpret the data and compare it with atmospheric models. To get the flux drop estimation, we used a formula to calculate the occultation depth caused by reflected light (by a Lambert surface, i.e. a surface which scatters intensity isotropically; e.g. Winn 2010):

$$\delta_{\rm occ,re} = A_g \left(\frac{R_p}{a}\right)^2, \tag{1}$$

where A_g is the wavelength dependent geometric albedo (ratio of the flux of a planet at full phase to the flux of a perfectly diffusing Lambert disc), R_p is the planetary radius and a is the semimajor axis of the orbit. For putting upper limits on occultation depths we assume A_g equal to one which sets the maximum possible value of the occultation depth due to reflected light.

During an occultation, the radiation flux of the system is decreased as the thermal radiation from the planet is no longer seen while the planet is behind the star. To include that, we used the following formulation to estimate the thermal contribution of the planet:

$$\delta_{\rm occ,th} = \left(\frac{R_p}{R_\star}\right)^2 \frac{B_\lambda(T_p)}{B_\lambda(T_\star)}, \tag{2}$$

where $R_\star$ is the stellar radius and B_λ (T_p, $T_\star$) are the Planck's functions corresponding to temperatures of the planet ($T_{\rm eq}$) and the star ($T_{\rm eff,\star}$), approximating them as blackbody radiators.

3.3 Estimation of temperatures

To estimate the equilibrium temperature of a planet we used this formula:

$$T_{\rm eq,p} = T_{\rm eff,\star}\sqrt{\frac{R_\star}{a}}\sqrt[4]{f(1-A_B)}. \tag{3}$$

[3]Available at https://github.com/nealegibson

Table 2. Results of the analysed data sets. Parameters presented and their meaning is following: the used HAWK-I filter, RMS_w is the standard deviation of the weighted mean of the binned data sets, $\delta_{occ,\,re,\,exp}$ is the expected occultation depth due to reflected light, $\delta_{occ,\,th,\,exp}$ is the expected occultation depth due to thermal radiation, $\delta_{occ,\,exp}$ is the total expected occultation depth (the sum of the both previous), δ_{occ} is the derived occultation depth (with at least 3σ significance), $\delta_{occ,3\sigma UL}$ is the 3σ upper limit on the occultation depth, and A_g is the upper limit (or derived value) of the geometric albedo. For *TESS* data sets δ_{tra} is the inferred transit depth. In the third table $T_{eq,\,p}$ is the equilibrium temperature of the planet.

TESS data sets

System	δ_{tra} (ppt)	RMS_w (ppt)	$\delta_{occ,\,re,\,exp}$ [a] (ppt)	$\delta_{occ,\,th,\,exp}$ [b] (ppt)	$\delta_{occ,\,exp}$ (ppt)	δ_{occ} (ppt)	A_g	$\delta_{occ,\,3\sigma UL}$ (ppt)	$A_{g,\,3\sigma UL}$
WASP-18	$10.617^{+0.014}_{-0.015}$	0.042	0.690	0.327[c]	1.017	$0.345^{+0.011}_{-0.011}$	$0.025^{+0.027}_{-0.027}$ [d]	–	<0.045[d]
WASP-36	$18.670^{+0.130}_{-0.130}$	0.288	0.500	0.012	0.512	$0.105^{+0.057}_{-0.049}$	$0.181^{+0.112}_{-0.096}$	<0.159	<0.286
WASP-43	$26.597^{+0.078}_{-0.070}$	0.148	0.990	0.007	0.997	$0.123^{+0.059}_{-0.048}$	$0.116^{+0.059}_{-0.048}$	<0.161	<0.154
WASP-50	$19.502^{+0.085}_{-0.093}$	0.174	0.340	0.002	0.342	$0.117^{+0.051}_{-0.048}$	$0.344^{+0.156}_{-0.148}$	<0.149	<0.440
WASP-51	$10.872^{+0.055}_{-0.055}$	0.105	0.263	0.004	0.267	$0.048^{+0.033}_{-0.024}$	$0.197^{+0.149}_{-0.109}$	<0.086	<0.368

VLT HAWK-I data set

System	Filter	RMS_w (ppt)	$\delta_{occ,\,re,\,exp}$(ppt)[a]	$\delta_{occ,\,th,\,exp}$ (ppt)[b]	$\delta_{occ,\,exp}$(ppt)	δ_{occ}(ppt)
WASP-43	NB2090	0.298	0.990	0.750	1.740	$1.26^{+0.17}_{-0.17}$

Planet:	WASP-18 b	WASP-36 b	WASP-43 b	WASP-50 b	WASP-51 b
T_{eq} (K)[e]	2504^{+63}_{-65}	1724^{+43}_{-43}	1439^{+34}_{-31}	1393^{+42}_{-42}	1637^{+42}_{-42}

[a]Calculated from equation (1) supposing $A_g = 1$; [b]calculated from equation (2) substituting $T_p = T_{eq,\,p}$ and $T_\star = T_{eff,\,\star}$; [c]adopted from Arcangeli et al. (2018), as in Shporer et al. (2019); [d]derived using the thermal contribution from Arcangeli et al. (2018), as in Shporer et al. (2019); [e]calculated from equation (3) assuming $f = 1/4$ and $A_B = 0$.

Here, $T_{eff,\,\star}$ is the effective temperature of the parent star, $R_\star$ is its radius, A_B is the Bond albedo (including radiation at all frequencies scattered into all directions), and f is a flux correction factor connected with redistribution of the stellar radiation over the planet's hemispheres.

Knowing the occultation depth from our fit and approximating planets and stars to be blackbody radiators, the brightness temperature T_b can be calculated from the occultation depth δ_{occ} as follows:

$$T_b(\lambda) = \left(\frac{hc}{\lambda k_B}\right)\left[\ln\left(1 + \frac{2hc^2k^2}{\delta_{occ}\lambda^5 B_{\lambda,\star}}\right)\right]^{-1}, \quad (4)$$

where h is Planck's constant, c is the speed of light in vacuum, k_B is the Steffan–Boltzmann constant, λ is the wavelength at which we observed, δ_{occ} is the measured occultation depth, and $B_{\lambda,\star}$ is the Planck function corresponding to T_{eff} of the star. We have also denoted $k^2 \equiv (R_p/R_\star)^2$ and used the wavelength dependent form of the Planck's law.

4 RESULTS

Following the methods described in Section 3, in Section 4.1 we describe our results for the *TESS* phase curves for each hot Jupiter target and in Section 4.2 for the HAWK-I occultation for WASP-43 b.

4.1 *TESS* phase curve models and upper limits

We were able to detect primary transits of all the systems in the *TESS* data sets. We have also detected the occultation of WASP-18 b, which has the brightest host star among the systems we consider here. For the other systems, we were able to place upper limits on their occultation depths and corresponding upper limits on their geometric albedos. For each binned data set we have also calculated the standard deviation of the weighted mean (RMS_w), serving as a measure of the quality of the data set and which can also be compared with expected and derived occultation depths.

To derive 3σ upper limits on the occultation depths of WASP-36 b, WASP-43 b, WASP-50 b, and WASP-51 b, we took values of the upper and the lower uncertainties of the derived occultation depth, averaged them, and multipied by three (i.e. $3[(\sigma_+ + \sigma_-)/2]$). A corresponding upper limit on the geometric albedo can be obtained using equation (1) and by estimating the contribution of reflected light, $\delta_{occ,\,re}$, to the observed occultation depth. To do this, we use equation (2) to estimate the contribution of thermal emission to the occultation depth, and subtract it from the observed occultation depth: $\delta_{occ,\,re} = \delta_{occ} - \delta_{occ,\,th}$.

In Table 2, we summarize our constraints on the transit/occultation depths and geometric albedos of each planet. We also show 'expected' values of the occultation depth for each planet ($\delta_{occ,\,exp}$), calculated as the sum of the 'expected' occultation depths due to reflected light ($\delta_{occ,\,re,\,exp}$) and thermal emission ($\delta_{occ,\,th,\,exp}$). These contributions are defined by equations (1) and (2), respectively, assuming a limiting case of $A_g = 1$ and $T_p = T_{eq,\,p}$, where $T_{eq,\,p}$ is defined according to equation (3) with $f = 0.25$ and $A_B = 0$. For all five hot Jupiters considered here, the occultation depth constraint (whether a detection or an upper limit) is lower than the 'expected' occultation depth due to reflection alone, $\delta_{occ,\,re,\,exp}$. This indicates that $A_g < 1$ for these planets, as expected given existing constraints on hot Jupiter albedos (e.g. Esteves et al. 2015). Fig. 2 shows our derived geometric albedo constraints as a function of a/R_p for all the planets studied in this work, alongside existing optical albedo constraints from the literature. The ratio a/R_p can be used to identify how well an exoplanet fits the characteristics of a hot Jupiter; a lower value means that the planet is closer to its parent star and/or has a larger radius.

In Fig. 3, we show geometric albedo as a function of equilibrium temperature for the same planets as in Fig. 2. The geometric albedo upper limits which we derive in this work for WASP-18 b, WASP-36 b, WASP-43 b, WASP-50 b, and WASP-51 b all lie below 0.45. This is consistent with previous works which find that hot Jupiters typically have low albedos (e.g. Heng & Demory 2013; Esteves et al. 2015; Mallonn et al. 2019; Brandeker et al. 2022), though higher optical albedos have also been measured in some cases (e.g. Esteves et al. 2015; Niraula et al. 2018; Wong et al. 2020b; Adams et al. 2021; Heng, Morris & Kitzmann 2021). The geometric albedos shown in Fig. 3 are consistent with a range of values, with upper limits spanning $\lesssim 0.05$ to $\sim$0.45. The diversity seen in hot Jupiter albedos may be indicative of a variety of cloud types and processes (Adams et al. 2021). Future albedo measurements spanning a wider range of equilibrium temperatures will be needed to further elucidate the nature of optical scattering in hot Jupiter atmospheres.

In what follows, we describe our results from the *TESS* data for each planet in turn. The estimated values of the fitted parameters are shown in Table 3, alongside the fixed parameters. In Table 4, we summarize the parameters subsequently derived from the best-fitting

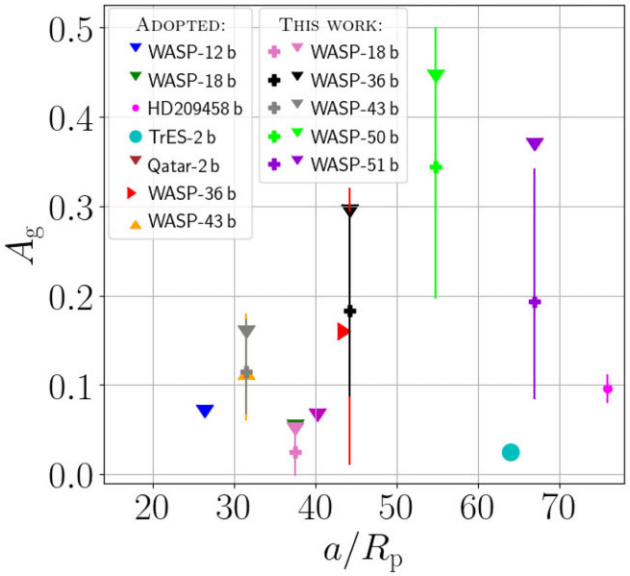

Figure 2. Optical geometric albedo as a function of the semimajor axis to planetary radius ratio, a/R_p. We include albedo constraints from the literature for seven hot Jupiters ('Adopted') as well as the *TESS* albedos derived here for WASP-18 b, WASP-36 b, WASP-43 b, WASP-50 b, and WASP-51 b ('This work'). The downward triangles (▼) show upper limits while a different symbol (bold ' + ' for our results) with an error bar shows a derived value including uncertainties. Literature references and corresponding instruments used are WASP-12 b: Bell et al. (2017), *HST* STIS; WASP-18 b: Shporer et al. (2019), *TESS*; HD 209458 b: Brandeker et al. (2022), *CHEOPS*; TrES-2 b: Kipping & Spiegel (2011), *Kepler*; Qatar-2 b: Dai et al. (2017), *K2 (Kepler)*; WASP-36 b & WASP-43 b: Wong et al. (2020b), *TESS*.

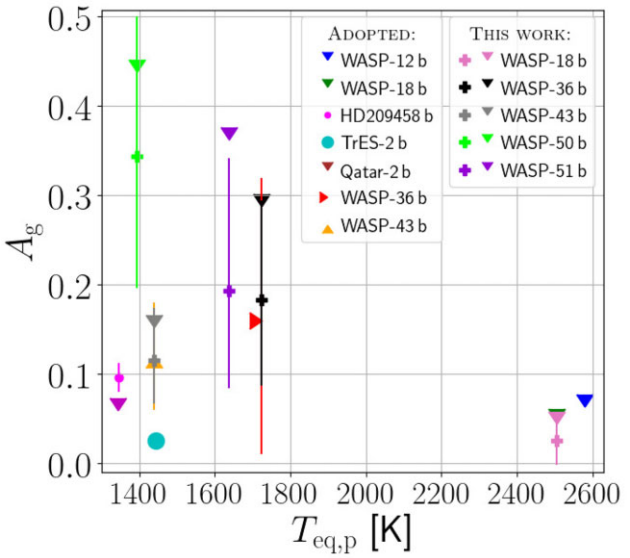

Figure 3. Optical geometric albedo as a function of equilibrium temperature, $T_{eq,\,p}$, for the same planets as in Fig. 2. Meaning of the used symbols, literature references and instruments used are the same as in Fig. 2.

phase curve parameters. Figs 4 and 5 show the fitted phase curves and occultations, respectively.

4.1.1 WASP-18

The *TESS* phase curve of this system has previously been studied by Shporer et al. (2019), as well as Günther & Daylan (2021) who also used ALLESFITTER to fit the phase curve. We detected a primary transit depth of $10.617^{+0.014}_{-0.015}$ ppt and an occultation depth of 0.345 ± 0.011 ppt. The occultation depth is consistent with the values derived by both Shporer et al. (2019) and Günther & Daylan (2021), while the primary transit depth we derive is consistent with that of Günther & Daylan (2021). Shporer et al. (2019) obtain a transit depth of $9.439^{+0.027}_{-0.026}$ ppt; the discrepancy between our value and theirs may be due to different analysis methods and the fact that we used data from four *TESS* sectors, while only two sectors were available at the time of their study. We determined the amplitude of the atmospheric contribution to the phase-curve model to be 0.3065 ± 0.0086 ppt (i.e. a semi-amplitude of 0.1533 ± 0.0043 ppt), which lies between the values derived by Günther & Daylan (2021) and Shporer et al. (2019). Furthermore, our value is consistent with that of Günther & Daylan (2021) to within 2σ, which is expected since ALLESFITTER was used for both analyses.

We further estimate the optical albedo of WASP-18 b based on the measured occultation depth. Due to the high dayside temperature of WASP-18 b, its thermal emission represents a non-negligible contribution in the *TESS* band, unlike the cooler targets in our sample. The way in which this thermal contribution is estimated may therefore have a significant effect on the resulting albedo constraint. Using equation (2), the thermal contribution to the occultation depth in the *TESS* band is 97 ppm, resulting in an albedo value of $A_g = 0.340 \pm 0.044$. This albedo calculation assumes efficient day–night energy redistribution ($f = 0.25$) in the estimation of T_p. However, existing infrared observations of WASP-18 b indicate that its day–night energy redistribution is inefficient (e.g. Arcangeli et al. 2018, see also Section 5).

A more accurate albedo constraint can be derived by considering a more realistic thermal contribution to the *TESS* occultation depth. Shporer et al. (2019) used the atmospheric model of Arcangeli et al. (2018), found by fitting the *HST* and *Spitzer* occultation depths of WASP-18 b and resulting in a thermal contribution of 0.327 ppt. As noted by Shporer et al. (2019), this contribution is consistent with the observed occultation depth, meaning that only an upper limit can be placed on the reflected contribution. They placed a 2σ upper limit of $A_g < 0.048$. To derive the geometric albedo, we used our value of the detected occultation depth and their value of the thermal contribution of 0.327 ppt, and we come to $A_g = 0.025 \pm 0.027$ which is consistent with their value obtained from the upper limit on the occultation depth. The high values of the uncertainties are caused by uncertainties of the thermal contribution which are expected to be a few per cent using the model of Arcangeli et al. (2018) as in Shporer et al. (2019). Thus, we set them to be 5 per cent when calculating the geometric albedo uncertainties. However, as our detected occultation depth is very similar to theirs (0.345 versus 0.341 ppt), we can also not claim a detection of the reflected light since the difference between the thermal emission and our occultation depth is not at 3σ significance ($\sim 1.6\sigma$). We, therefore, set a 3σ uppper limit on the reflected light by the planet of <0.033 ppt implying an upper limit on the geometric albedo $A_g < 0.045$, consistent with the 2σ upper limit of Shporer et al. 2019.

We note that our self-consistent atmospheric model for WASP-18 b, discussed in Section 5, is consistent with the observed oc-

Table 3. Posterior values of all the fitted parameters (and hyperparameters) of *TESS* phase curves of all the systems analysed in this work obtained by using by ALLESFITTER Nested sampling.

Parameter/system	WASP-18	WASP-36	WASP-43	WASP-50	WASP-51	fit/fixed
$R_p/R_\star$	0.09669 ± 0.00013	0.13271 ± 0.00085	0.15865 ± 0.00044	0.13668 ± 0.00058	0.10949 ± 0.00046	fit
$(R_\star + R_p)/a$	0.3131 ± 0.0023	0.1952 ± 0.0044	0.2474 ± 0.0022	0.1550 ± 0.0022	0.1609 ± 0.0013	fit
$\cos i$	$0.0997^{+0.0059}_{-0.0063}$	0.1157 ± 0.0059	0.1481 ± 0.0027	0.0974 ± 0.0028	0.1214 ± 0.0013	fit
T_0 (epoch)	0.000021 ± 0.000035	-0.00002 ± 0.00014	0.000013 ± 0.000048	-0.000017 ± 0.000096	0.00004 ± 0.00012	fit
P (d)	0.9414518	1.5373653	0.81347753	1.9550959	2.8106084	fixed
$\sqrt{e}\cos\omega$	−0.00163718	0.0	0.05017120	0.06824257	−0.05781180	fixed
$\sqrt{e}\sin\omega$	−0.09379403	0.0	−0.03135045	0.06590108	−0.17792638	fixed
J_{TESS}	0.0041 ± 0.0012	$0.0019^{+0.0024}_{-0.0013}$	$0.0032^{+0.0022}_{-0.0018}$	$0.0035^{+0.0029}_{-0.0021}$	$0.0037^{+0.0026}_{-0.0021}$	fit
$q_{1;\ TESS}$	0.36660057	0.38667813	0.53140888	0.44026143	0.37665187	fixed
$q_{2;\ TESS}$	0.15570471	0.15819508	0.10952400	0.13763435	0.1549222	fixed
$\ln\sigma_{TESS}$ [ln(relative flux)]	-10.075 ± 0.043	-7.774 ± 0.034	-8.605 ± 0.048	-8.245 ± 0.030	-8.732 ± 0.026	fit
ΔF_{TESS}	-0.0002474 ± 0.0000076	$0.000141^{+0.000038}_{-0.000040}$	$0.000161^{+0.000025}_{-0.000027}$	$0.000050^{+0.000017}_{-0.000019}$	0.0000334 ± 0.0000099	fit
$A_{p;\ beaming;\ TESS}$ [ppt] (semi-amplitude)	0.0312 ± 0.0035	$0.032^{+0.024}_{-0.018}$	$0.0157^{+0.013}_{-0.0096}$	$0.033^{+0.015}_{-0.014}$	$0.0139^{+0.0074}_{-0.0069}$	fit
$A_{p;\ atmospheric;\ TESS}$ [ppt] (amplitude)	0.3065 ± 0.0086	$0.062^{+0.049}_{-0.036}$	$0.037^{+0.030}_{-0.022}$	$0.044^{+0.030}_{-0.024}$	$0.0031^{+0.0042}_{-0.0022}$	fit
$A_{p;\ ellipsoidal;\ TESS}$ [ppt] (amplitude)	0.3516 ± 0.0089	$0.099^{+0.058}_{-0.050}$	0.085 ± 0.037	$0.0084^{+0.0110}_{-0.0057}$	$0.026^{+0.016}_{-0.014}$	fit

Table 4. Posterior values of all the derived parameters of *TESS* phase curves of all the systems analysed in this work obtained by using by ALLESFITTER Nested Sampling.

Parameter/system	WASP-18	WASP-36	WASP-43	WASP-50	WASP-51
Host star radius over semimajor axis; $R_\star/a$	0.2855 ± 0.0021	0.1723 ± 0.0038	0.2135 ± 0.0018	0.1364 ± 0.0019	0.1450 ± 0.0012
Semimajor axis over host star radius; $a/R_\star$	3.502 ± 0.025	$5.80^{+0.13}_{-0.12}$	4.683 ± 0.041	7.33 ± 0.11	6.895 ± 0.056
Planetary radius over semimajor axis; R_p/a	0.02761 ± 0.00023	0.02286 ± 0.00062	0.03388 ± 0.00037	0.01864 ± 0.00033	0.01588 ± 0.00018
Planetary radius; R_p ($R_\oplus$)	13.29 ± 0.42	13.6 ± 2.5	11.54 ± 0.18	13.1 ± 1.6	15.89 ± 0.37
Planetary radius; R_p (R_J)	1.186 ± 0.038	1.21 ± 0.22	1.030 ± 0.016	1.17 ± 0.15	1.417 ± 0.033
Semimajor axis of the planetary orbit; a ($R_\odot$)	4.41 ± 0.14	5.46 ± 1.0	3.124 ± 0.054	6.45 ± 0.81	9.17 ± 0.22
Semimajor axis of the planetary orbit; a (AU)	0.02052 ± 0.00067	0.0254 ± 0.0047	0.01453 ± 0.00025	0.0300 ± 0.0038	0.0427 ± 0.0010
Inclination angle of the planetary orbit; i (deg)	$84.28^{+0.37}_{-0.34}$	83.36 ± 0.34	81.49 ± 0.16	84.41 ± 0.16	83.026 ± 0.077
Impact parameter; b_{tra}	$0.352^{+0.018}_{-0.020}$	$0.671^{+0.018}_{-0.020}$	0.6946 ± 0.0069	$0.7099^{+0.0099}_{-0.0110}$	0.8651 ± 0.0029
Total transit duration; T_{tot} (h)	2.1956 ± 0.0041	1.867 ± 0.017	1.2552 ± 0.0058	1.810 ± 0.012	2.257 ± 0.011
Full-transit duration; T_{full} (h)	1.7486 ± 0.0043	$1.121^{+0.025}_{-0.027}$	0.6393 ± 0.0091	$1.000^{+0.018}_{-0.019}$	$0.686^{+0.037}_{-0.039}$
Epoch occultation; $T_{0;\ occ}$	0.470655 ± 0.000035	0.76867 ± 0.00014	0.408289 ± 0.000049	0.985589 ± 0.000096	1.38599 ± 0.00012
Impact parameter occultation; b_{occ}	$0.346^{+0.018}_{-0.020}$	$0.671^{+0.018}_{-0.020}$	0.6921 ± 0.0069	$0.7188^{+0.0100}_{-0.011}$	0.8093 ± 0.0027
Transit depth; $\delta_{tra;\ p;\ TESS}$ (ppt)	$10.617^{+0.014}_{-0.015}$	18.67 ± 0.13	$26.597^{+0.078}_{-0.070}$	$19.502^{+0.085}_{-0.093}$	10.872 ± 0.055
Occultation depth; $\delta_{occ;\ p;\ TESS}$ (ppt)	0.345 ± 0.011	$0.105^{+0.057}_{-0.049}$	$0.123^{+0.059}_{-0.048}$	$0.117^{+0.051}_{-0.048}$	$0.048^{+0.033}_{-0.024}$
Nightside flux of the planet; $F_{nightside;\ p;\ TESS}$ (ppt)	0.039 ± 0.011	$0.034^{+0.043}_{-0.023}$	$0.079^{+0.057}_{-0.043}$	$0.068^{+0.047}_{-0.041}$	$0.045^{+0.031}_{-0.025}$
Median host star density – all orbits; $\rho_\star$ (cgs)	0.917 ± 0.020	$1.564^{+0.11}_{-0.096}$	2.936 ± 0.077	$1.950^{+0.086}_{-0.080}$	0.785 ± 0.019

cultation depth within 2σ without the inclusion of scattering from clouds or hazes. The predicted thermal contribution from this model is slightly higher than the observed occultation depth, and is therefore consistent with zero albedo in the *TESS* band.

4.1.2 WASP-36

We detected the primary transit of WASP-36 b and obtained a transit depth of 18.67 ± 0.13 ppt. This value is lower than that obtained by Maciejewski et al. (2016) in the *R* band (19.349 ± 0.320 ppt); however, this difference may be due to the different wavelength range used. We obtained an occultation depth of $0.105^{+0.057}_{-0.049}$ ppt, and therefore did not significantly detect the occultation of WASP-36 b ($\sim 2\sigma$ detection). This is a result of the relatively high RMS_w of the data of 0.288 ppt. We place a 3σ upper limit on the occultation depth of $\delta_{occ} < 0.159$ ppt. This is consistent with the constraint from Wong et al. (2020b), who derive $\delta_{occ} = 0.09^{+0.10}_{-0.07}$ ppt using *TESS*. Zhou et al. (2015) derive an occultation depth of 1.3 ± 0.4 ppt in the *Ks* band; for the shorter wavelengths at which *TESS* operates, the occultation depth is indeed expected to be lower under the assumption of little or no optical scattering. The upper limit which we derive on the occultation depth corresponds to a 3σ upper limit on the geometric albedo of $A_g < 0.286$. This is consistent with the geometric albedo constraint derived by Wong et al. (2020b) ($A_g = 0.16^{+0.16}_{-0.15}$).

4.1.3 WASP-43

We detected the primary transit of WASP-43 b, obtaining a transit depth of $26.597^{+0.078}_{-0.070}$ ppt. This value is slightly different than 25.415 ± 0.131 ppt in the optical band ($i' + g'$ filters) published in Hoyer et al. (2016). We do not detect the occultation of WASP-43 b at sufficiently high significance, obtaining $\delta_{occ} = 0.123^{+0.059}_{-0.048}$ ppt (2.3σ) while the RMS_w of our data is 0.148 ppt. This is consistent with the results of Wong et al. (2020b), who obtain a *TESS* occultation depth of $\delta_{occ} = 0.17 \pm 0.07$ ppt. Furthermore, Chen et al. (2014) measured the occultation depth of WASP-43 b in the

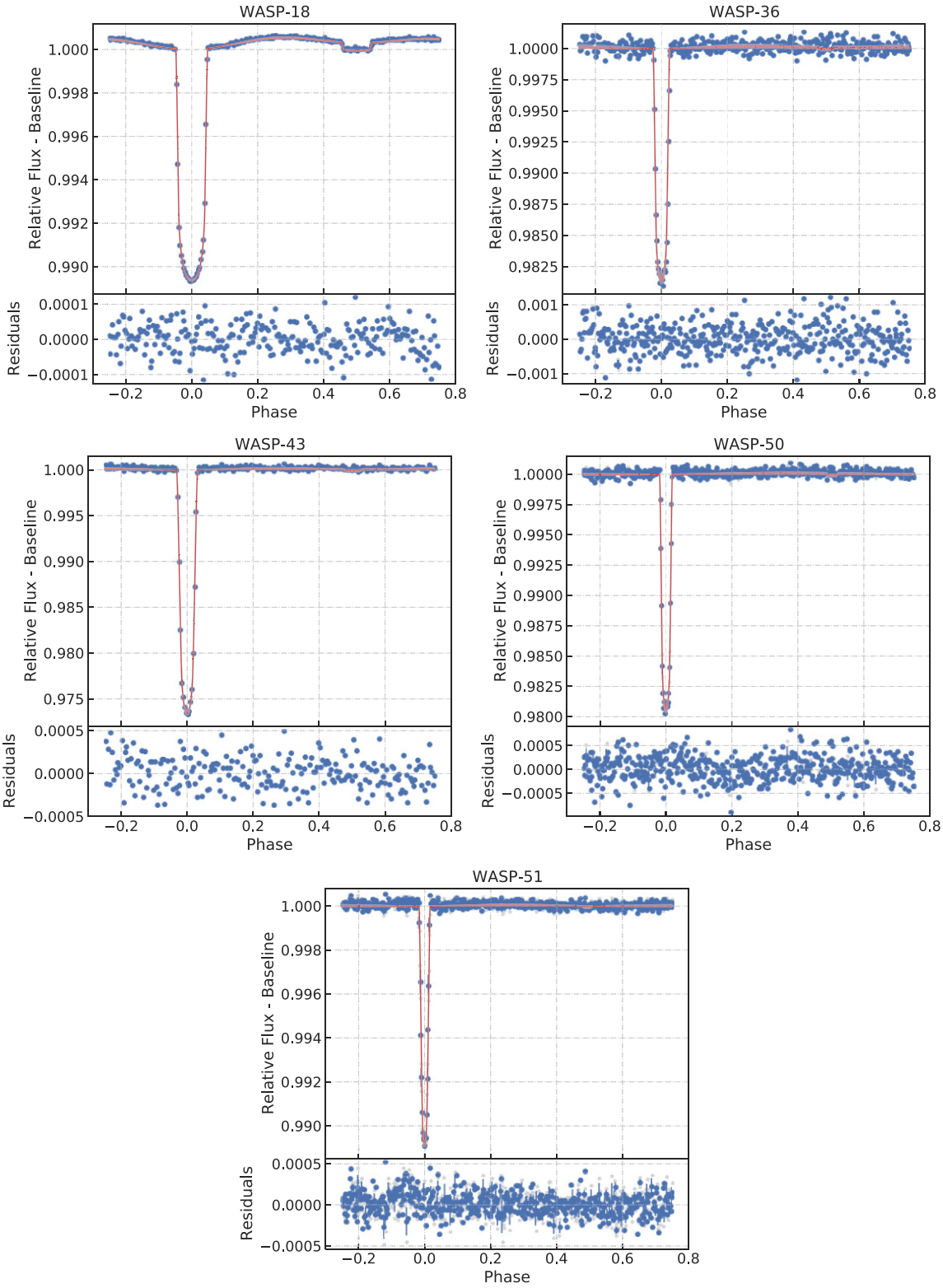

Figure 4. *TESS* phase curves fitted by ALLESFITTER software package. The light grey points are the original data binned per 5 min, the blue points with error bars (mostly not visible) are the data binned per 15 minutes, and the red curves (seen as one) show 50 models that are randomly drawn from the posteriors.

i' band (centred on roughly the same wavelength as the *TESS* bandpass) to be $\delta_{\rm occ} = 0.37 \pm 0.22$ ppt, which is also consistent with our value. Fraine et al. (2021) put for the reflected light component a 3σ upper limit $\delta_{\rm occ} < 0.067$ ppt from *HST* WFC3/UVIS data and from this value they derived a 3σ upper limit $A_{\rm g} \lesssim 0.06$. From our 3σ upper limit on the occultation depth of $\delta_{\rm occ}$

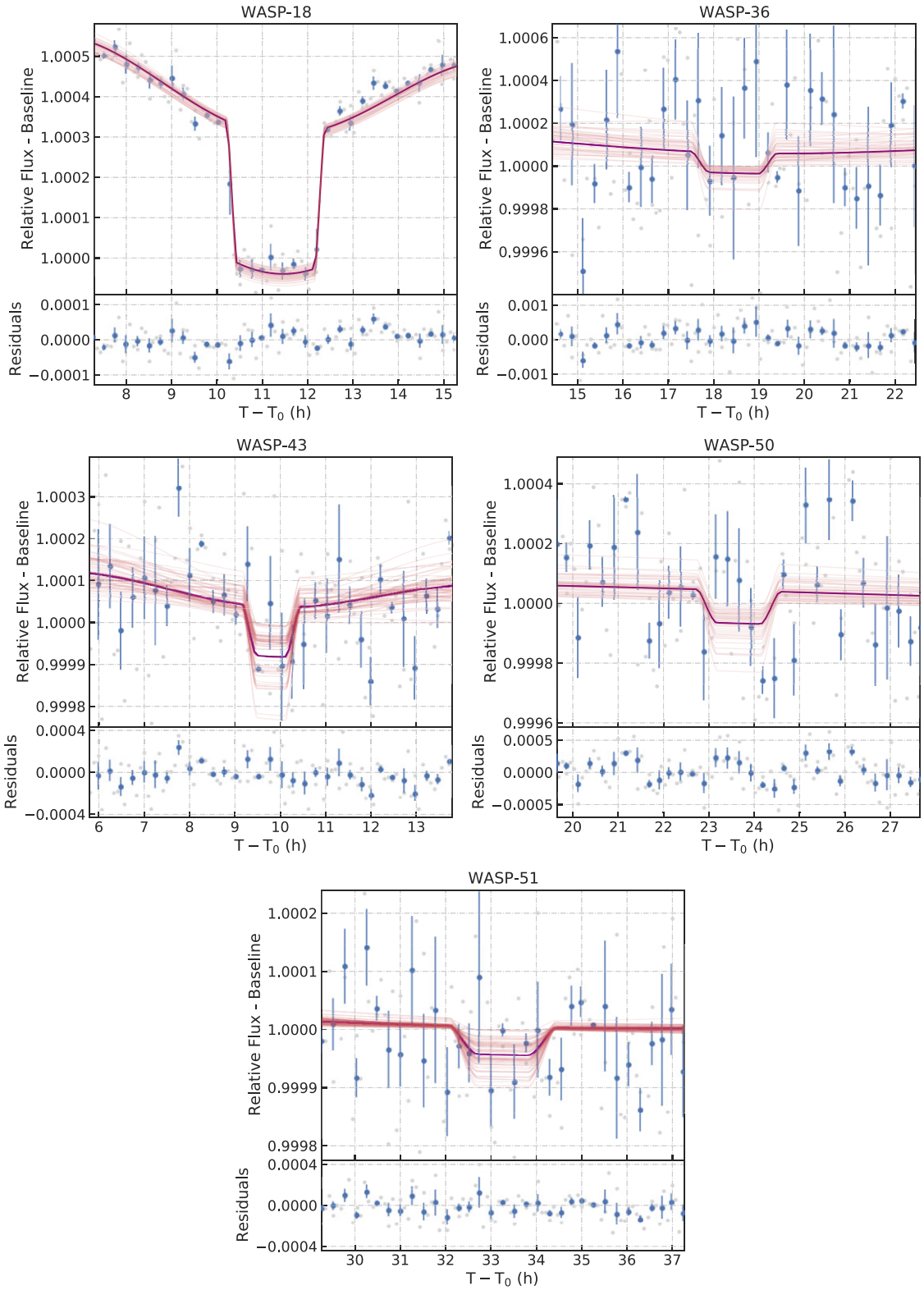

Figure 5. *TESS* phase curves fitted by ALLESFITTER software package with the occultation part zoomed. The purple curves show the median model drawn from the posteriors. The meaning of all the points and the red curves is the same as in Fig. 4.

$<$ 0.161 ppt, we derive an upper limit on the geometric albedo of $A_g < 0.154$. This value is consistent with the albedos derived by Wong et al. (2020b) and Chen et al. (2014), i.e. 0.12 $\pm$ 0.06 and 0.31 $\pm$ 0.22, respectively. Our δ_{occ} and A_g upper limits are also consistent with the upper limits obtained by Fraine et al. (2021).

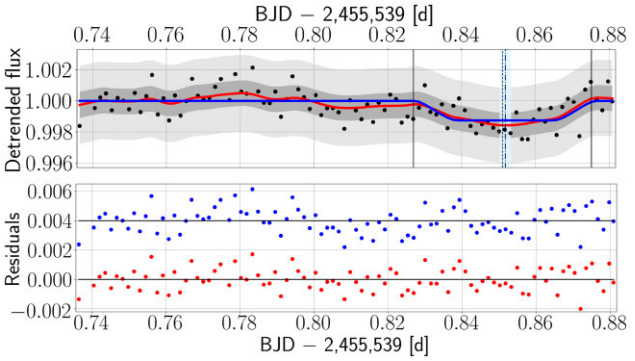

Figure 6. Results of the best-fitting model of WASP-43 from HAWK-I data. *The upper panel*: Detrended occultation light curve. The black dots are our measurements binned per 2 min, the red curve shows the fit of the data (the occultation model + noise model) together with 1σ and 3σ regions depicted as the shaded regions. The blue curve is the occultation model only. The black vertical lines show the calculated beginning, the centre, and the end of the occultation, and the blue dot-and-dash vertical line shows the inferred centre of the occultation together with 1σ uncertainty region (the light-blue area). *The bottom panel*: blue – residuals of the occultation model, red – residuals of the fit.

4.1.4 WASP-50

We obtained a transit depth value of $19.502^{+0.085}_{-0.093}$ ppt. This is consistent with the derived value of 19.321 ± 0.167 ppt in the *I* and *R* bands published in Chakrabarty & Sengupta (2019). We detected an occultation with less than 3σ significance, $\delta_{\rm occ} = 0.117^{+0.051}_{-0.048}$ ppt ($\sim 2.4\sigma$), which is nevertheless the first occultation measurement of this system. Our derived value is lower than the expected value of 0.342 ppt (assuming $A_g = 1$) and also lower than $\rm RMS_w$ of our data, 0.174 ppt. We placed a 3σ upper limit on the occultation depth $\delta_{\rm occ} < 0.149$ ppt. From the upper limit of the occultation depth, we then derived an upper limit on the geometric albedo of $A_{\rm g} < 0.44$.

4.1.5 WASP-51

We obtained a transit depth of 10.872 ± 0.055 ppt. While this value is not consistent with the transit depths derived by Maciejewski et al. (2016) and Saha, Chakrabarty & Sengupta (2021) in the *R* and *V* bands, respectively, the difference may be due to the use of different wavelength ranges. Indeed, Saeed, Goderya & Chishtie (2022) discovered a strong dependency of the transit depth with wavelength. The occultation of WASP-51 b was not detected at sufficiently high significance, with a measured occultation depth of $0.048^{+0.033}_{-0.024}$ ppt ($\sim 1.7\sigma$). As in the case of WASP-50, this the first occultation measurement of this system. The RMS of the data was also high, at 0.105 ppt. We placed an upper limit on the occultation depth $\delta_{\rm occ} < 0.086$ ppt. This allowed us to set a 3σ upper limit on the geometric albedo $A_{\rm g} < 0.368$ ppt.

4.2 HAWK-I occultation measurement for WASP-43 b

We detected the occultation of WASP-43 b using the HAWK-I NB2090 data described in Section 2.3.2, consistent with the detection by Gillon et al. (2012) who used the same data set but different analysis methods. Here, we first binned the near-infrared HAWK-I data by 2-min time intervals. As well as for the *TESS* data sets, we have calculated the $\rm RMS_w$. The fitted light curve is shown in Fig. 6. All used and inferred parameters are summarized in Table 5.

Table 5. Deduced, calculated, and fixed parameters of the occultation of WASP-43.

Deduced parameters	
Occultation depth $\delta_{\rm occ}$ (ppt)	$1.261^{+0.165}_{-0.168}$
$T_0 - 2,450\,000$ ($\rm BJD_{TDB}$)	$0.8519^{+0.0016}_{-0.0015}$
Out-of-occultation flux $f_{\rm oot}$	1.0027 ± 0.0003
Time gradient $T_{\rm grad}$	0.0013 ± 0.0005
Time gradient $T^2_{\rm grad}$	-0.0002 ± 0.0002
ξ (GP)	$0.0003877^{+0.0001523}_{-0.0001066}$
η_t (GP)	$0.0081001^{+0.0018084}_{-0.0015249}$
η_a (GP)	$0.0266166^{+0.0018885}_{-0.0017666}$
$\sigma^2_{\rm w}$ (GP)	$0.0007866^{+0.0000878}_{-0.0000703}$
Calculated parameters	
Equilibrium temperature[a] $T_{\rm eq}$ (K)	1439^{+34}_{-31}
Brightness temperature[b] $T_{\rm b}$ (K)	1619^{+47}_{-52}
Fixed parameters[c]	
Period P (d)	0.81347404
Scaled semimajor axis $a/R_\star$	5.13
Ratio of the radii $R_{\rm p}/R_\star$	0.159687
Impact parameter b	0.66

[a]Calculated from equation (3) assuming $f = 1/4$ and $A_{\rm B} = 0$; [b]calculated from equation (4); [c]taken from Hellier et al. (2011).

We detected the occultation of WASP-43 b and inferred an occultation depth, $\delta_{\rm occ}$, of 1.26 ± 0.17 ppt. The inferred time of the occultation centre is consistent with the expected value within the derived uncertainty. Our $\delta_{\rm occ}$ value is consistent with the value of Gillon et al. (2012) (1.56 ± 0.14 ppt) within 1.8σ. Our inferred occultation depth of 1.26 ± 0.17 ppt is significantly deeper than our *TESS* occultation depth upper limit of 0.161 ppt. This implies that planet-star flux ratio is increasing with wavelength, which is naturally explained by the decreasing stellar flux and increasing planetary thermal emission with wavelength in the near-infrared.

We use this occultation depth to calculate the brightness temperature of WASP-43 b at $\sim 2.09\,\mu$m, obtaining a value of $T_{\rm b} = 1619 \pm 52$ K. This temperature can be used to gain some initial insights into the energy redistribution in the atmosphere of WASP-43 b. For example, the equilibrium temperature of WASP-43 b assuming zero albedo and a flux correction factor, f, of 1/4 is $T_{\rm eq} = 1439 \pm 34$ K (see equation 3). The brightness temperature corresponding to the HAWK-I occultation is greater than $T_{\rm eq}$, which may be due to inefficient day–night energy redistribution (i.e. $f > 1/4$). A lower limit on the efficiency of day–night energy redistribution can be estimated by substituting $T_{\rm b} - \sigma_{T_{\rm b}}$ for $T_{\rm eq,\,p}$ in equation (3) and solving for f. We obtain a physically plausible estimate of $f \geq 0.35$, which lies between the limits of $f = 1/4$ (uniform redistribution) and $f = 2/3$ (instantaneous reradiation). This is consistent with the result obtained by Chen et al. (2014) of $f \geq 0.56$, measured in the *K* band.

While optical observations can be used to estimate the optical albedos of hot Jupiter atmospheres, inferring infrared scattering can be more complex. In the near-infrared, thermal emission dominates the observed planetary flux and is expected to be significantly greater than the contribution from reflected light. Furthermore, molecular opacity in the infrared causes the planetary thermal emission to significantly deviate from a blackbody spectrum, as can be seen from the evident H_2O absorption in the *HST*/WFC3 spectrum of WASP-43 b (Kreidberg et al. 2014). As a result, the method described in Section 4.1 to estimate optical geometric albedos should not be used in the near-infrared. Instead, detailed radiative-convective atmo-

spheric models can be used to explain multiwavelength observations and assess the need for optical and/or infrared scattering. We do this for WASP-43 b and WASP-18 b in Section 5, and find that cloud scattering is not required to explain either of their optical to infrared spectra.

While our self-consistent atmospheric models indicate that cloud scattering is not needed to explain the optical and infrared observations of WASP-43 b, Keating & Cowan (2017) find that an infrared albedo of 0.24 ± 0.01 is needed to fit the *HST*/WFC3 and *Spitzer* observations. However, we note that their atmospheric model assumes an isothermal temperature profile, which does not capture the effect of molecular absorption features. In contrast to this, we find that the *HST*/WFC3 and *Spitzer* data can be explained by absorption features due to H_2O and CO (see Section 5). This highlights the need to consider molecular spectral features when interpreting infrared observations. Nevertheless, in order to compare with the results of Keating & Cowan (2017), we use the HAWK-I occultation depth derived above to estimate a nominal infrared albedo. As in Keating & Cowan (2017), we assume a blackbody thermal contribution to the observed planetary flux. We use a planetary temperature of 1483 K, i.e. the best-fitting isothermal temperature found by Keating & Cowan (2017). Using equation (2), this results in a nominal thermal contribution of 0.864 ppt. Following the methods outlined in Section 4.1, this results in an estimated infrared albedo of $A_g = 0.395^{+0.174}_{-0.176}$. Our nominal albedo estimate agrees with the results of Keating & Cowan (2017) when the same assumptions are made. However, we stress that the infrared thermal contribution should not be assumed to take the form of a blackbody, and that detailed atmospheric models are required to interpret infrared observations. We discuss our self-consistent models in Section 5.

5 ATMOSPHERIC CONSTRAINTS FOR WASP-43 B AND WASP-18 B

WASP-43 b and WASP-18 b represent opposite ends in temperature across the hot and ultra-hot Jupiter regimes. Therefore, they are ideal case studies for the comparative study of hot Jupiter atmospheres, including the presence of clouds and hazes. The *TESS* and HAWK-I occultation depths we have derived for these planets (Section 4) provide constraints on the optical and near-infrared thermal emission/scattering of these planets. In this section, we therefore model the atmospheres of WASP-43 b and WASP-18 b in order to assess their potential atmospheric properties.

We self-consistently model the dayside atmospheres of WASP-43 b and WASP-18 b using the GENESIS atmospheric model (Gandhi & Madhusudhan 2017; Piette et al. 2020). GENESIS solves for the temperature profile, thermal emission spectrum and chemical profile of the atmosphere by calculating full, line-by-line radiative transfer under radiative-convective, thermodynamic, hydrostatic and thermochemical equilibrium. In particular, equilibrium chemical abundances are calculated using the HSC CHEMISTRY (version 8) software (see e.g. Moriarty, Madhusudhan & Fischer 2014; Harrison, Bonsor & Madhusudhan 2018; Piette et al. 2020). HSC CHEMISTRY minimizes the Gibbs' free energy of the system using the GIBBS solver (White, Johnson & Dantzig 1958), given the atmospheric elemental abundances. These equilibrium chemistry calculations consider >150 chemical species (see Piette et al. 2020). Of these, we consider atmospheric opacity due to the species known to dominate the H_2-rich atmospheres of hot Jupiters (Burrows & Sharp 1999; Madhusudhan et al. 2016): H_2O, CH_4, CO, CO_2, NH_3, HCN, C_2H_2, Na, K, TiO, VO and H^-, besides H_2 and He. We note that besides Na, K, TiO, and VO, other atomic and molecular species such as Fe and AlO can also contribute to the optical opacity and cause thermal inversions in hot Jupiter atmospheres (e.g. Lothringer et al. 2018; Gandhi & Madhusudhan 2019). However, the optical data considered here (i.e. *TESS* photometry) is only sensitive to the integrated optical flux, and does not resolve spectral features due to individual species. We therefore use Na, K, TiO, and VO as a proxy for the atmospheric optical opacity in these models, and find that we are able to explain the observations.

We calculate the absorption cross-sections of these species as in Gandhi & Madhusudhan (2017) using line lists from ExoMol, HITEMP, and HITRAN (H_2O, CO, and CO_2: Rothman et al. 2010; CH_4: Yurchenko et al. 2013, Yurchenko & Tennyson 2014; C_2H_2: Rothman et al. 2013, Gordon et al. 2017; NH_3: Yurchenko, Barber & Tennyson 2011; HCN: Harris et al. 2006, Barber et al. 2014; TiO: McKemmish et al. 2019; VO: McKemmish, Yurchenko & Tennyson 2016; H_2-H_2 and H_2-He collision-induced absorption: Richard et al. 2012). Na and K opacities are calculated as in Burrows & Volobuyev (2003) and Gandhi & Madhusudhan (2017), and H^- bound-free and free–free cross-sections are calculated using the prescriptions of Bell & Berrington (1987) and John (1988) (see also Arcangeli et al. 2018; Parmentier et al. 2018; Gandhi et al. 2020).

The free parameters in the atmospheric model are therefore the elemental abundances (explored here by changing the C/O ratio and metallicity), the incident irradiation, and the internal flux. The incident irradiation on the dayside of a hot Jupiter can be varied by considering different efficiencies of energy redistribution, both on the dayside and between the day and nightsides (see e.g. Burrows, Budaj & Hubeny 2008a), as described below. The internal flux can be parametrized by a single temperature parameter (T_{int}) and represents the flux emanating from the planetary interior, e.g. as a remnant of the planet formation process. Given the relatively high irradiation levels of both WASP-43 b and WASP-18 b, the internal heat is not expected to noticeably affect the observable atmosphere. We therefore set T_{int} to a nominal value of 100 K, similar to that of Jupiter. We explore physically plausible models for WASP-43 b and WASP-18 b in order to explain their observed *TESS* and HAWK-I occultation depths (reported in this work) as well as existing *Spitzer* IRAC dayside fluxes. The IRAC 1 and IRAC 2 data are obtained from Blecic et al. (2014) and Sheppard et al. (2017) for WASP-43 b and WASP-18 b, respectively.

For WASP-43 b, we find that an atmospheric model with solar metallicity and C/O = 0.5 is able to fit the observed *TESS*, HAWK-I and *Spitzer* data if 10 per cent of the energy incident on the dayside is transported to the nightside, and energy redistribution is efficient on the dayside (the top panel of Fig. 7). Using the notation of Burrows et al. (2008a) and equation (3), this corresponds to a flux distribution factor of $f = 0.45$. Our model is in agreement with previous inferences of inefficient day–night energy redistribution from *Spitzer* and TRAPPIST eclipse observations (Gillon et al. 2012; Blecic et al. 2014). The strong day–night flux contrast from *Spitzer* phase curve constraints is also suggestive of inefficient day–night energy redistribution (Stevenson et al. 2014, 2017), though Stevenson et al. (2017) note that this contrast could also be caused by high-altitude nightside clouds. Our model fits the *Spitzer* and HAWK-I NB2090 data within the $\sim 1\sigma$ uncertainties, while models with more efficient day–night energy redistribution result in IRAC 1 and IRAC 2 brightness temperatures that are colder than what is observed.

This atmospheric model for WASP-43 b is dominated by H_2O and CO opacity, as expected for H_2-rich atmospheres at such temperatures (Burrows & Sharp 1999; Madhusudhan et al. 2016). The IRAC 1 and IRAC 2 bands probe H_2O and CO absorption

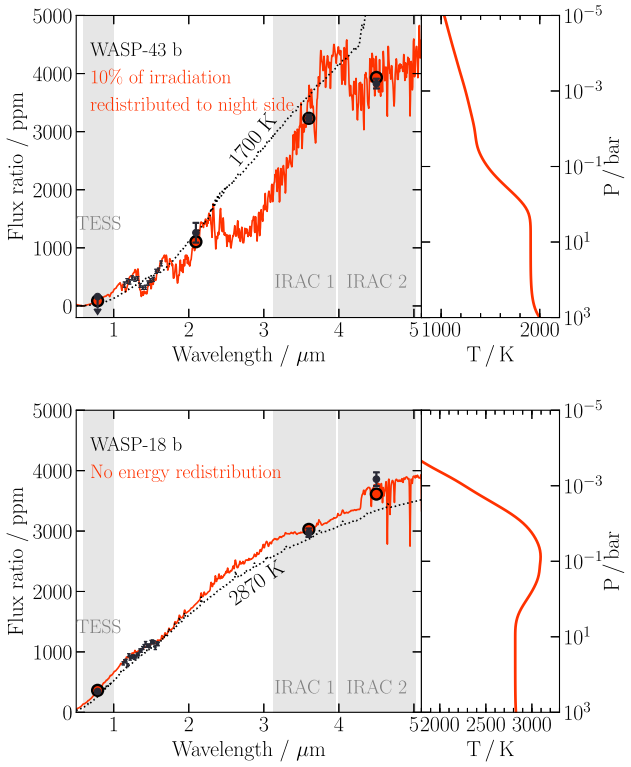

Figure 7. Self-consistent temperature profiles and thermal emission spectra for the dayside atmospheres of WASP-43 b (top panel) and WASP-18 b (bottom panel). *TESS*, HAWK-I and *Spitzer* observations (upper limits) are shown as black points and error bars (arrows), while the red circles show the binned model points. Note that the *TESS* error bar for WASP-18 b is smaller than the symbol size. The *Spitzer* data for WASP-43 b and WASP-18 b are from Blecic et al. (2014) and Sheppard et al. (2017), respectively. Small black points and error bars show *HST*/WFC3 data for WASP-43 b (Kreidberg et al. 2014) and WASP-18 b (Sheppard et al. 2017). The dashed black lines show blackbody spectra corresponding to the irradiation temperature, $T_{\rm irr}$, for each planet. $T_{\rm irr} = 2^{-1/4}\sqrt{R_\star/a}\,T_{{\rm eff},\star}$ corresponds to the dayside temperature of the planet assuming no day–night energy redistribution and a Bond albedo of zero ($R_\star$, a, and $T_{{\rm eff},\star}$ defined as in Section 3).

features, respectively. Meanwhile, the *TESS* and HAWK-I NB2090 bands probe the spectral continuum and therefore have a higher brightness temperature relative to the *Spitzer* data. The model also agrees well with occultation data from the *Hubble Space Telescope*'s Wide-Field Camera 3 (*HST*/WFC3; Kreidberg et al. 2014), as shown in Fig. 7. We further note that the *TESS* upper limit is consistent with pure thermal emission, without the need for reflected light.

In the case of WASP-18 b, we find that an atmospheric model with solar metallicity and C/O = 1 is able to fit the observed *TESS* and *Spitzer* data if there is no day–night energy redistribution and no energy redistribution on the dayside of the planet (i.e. instant re-radiation). This corresponds to a flux distribution factor of $f = 2/3$ (Burrows et al. 2008a) and is consistent with *Spitzer* phase curve observations (Maxted et al. 2013), while Arcangeli et al. (2019) infer a redistribution efficiency between uniform dayside redistribution ($f = 0.5$) and instant re-radiation ($f = 2/3$) from *HST*/WFC3 phase curve observations. The model is shown in the bottom panel of Fig. 7 and is able to fit the *TESS* and *Spitzer* observations within the $\sim 2\sigma$ uncertainties.

This atmospheric model for WASP-18 b is also broadly consistent with previous studies of its *Spitzer* and *HST*/WFC3 thermal emission observations (Sheppard et al. 2017; Arcangeli et al. 2018; Gandhi et al. 2020). For example, Sheppard et al. (2017) retrieve C/O = 1, while Gandhi et al. (2020) find evidence for sub-solar H_2O and super-solar CO (consistent with a high C/O ratio) and Arcangeli et al. (2018) derive a super-solar upper limit of C/O < 0.85. Furthermore, the atmospheric metallicity derived by Arcangeli et al. (2018) is consistent with solar values, though Sheppard et al. (2017) infer a super-solar metallicity and Gandhi et al. (2020) infer a metallicity between solar and super-solar, depending on the model assumptions and data used. We overplot the *HST*/WFC3 data from Sheppard et al. (2017) in Fig. 7 and find that these are in good agreement with our self-consistent model. We note that the photometric *TESS* and *Spitzer* data is not significantly sensitive to the model C/O ratio, while the lack of H_2O absorption in the *HST*/WFC3 data is better fit by a higher C/O ratio. Consistent with Sheppard et al. (2017), Arcangeli et al. (2018), and Gandhi et al. (2020), we find that a thermal inversion is required to explain the *Spitzer* data for WASP-18 b. In particular, the IRAC 2 data point probes a CO emission feature and therefore has a higher brightness temperature than the *TESS* and IRAC 1 observations. Furthermore, we find that with this model, the *TESS* observation is readily explained by thermal emission alone, without the need for reflected light.

6 CONCLUSIONS

In this work, we have presented constraints on the occultation depths and geometric albedos ($A_{\rm g}$) of five hot Jupiters using data from the *TESS* space mission: WASP-18 b, WASP-36 b, WASP-43 b, WASP-50 b, and WASP-51 b. We place the first constraints on the albedos of WASP-50 b and WASP-51 b, i.e. 3σ upper limits of $A_{\rm g} < 0.44$ and $A_{\rm g} < 0.368$, respectively. For WASP-36 b, we place a 3σ upper limit of $A_{\rm g} < 0.286$, consistent with the previously published value of 0.16 ± 0.16 (Wong et al. 2020a). We further confirm the previous transit and occultation detections of WASP-18 b with *TESS*, and find a 3σ upper limit on the albedo, $A_{\rm g} < 0.045$, consistent with the result of Shporer et al. (2019). We also place a 3σ upper limit on the albedo of WASP-43 b, $A_{\rm g} < 0.154$, in the *TESS* bandpass, consistent with the results of Chen et al. (2014) and Wong et al. (2020a).

Using data of the ground-based ESO VLT HAWK-I near-infrared instrument, we confidently detect the occultation of WASP-43 b. This data point is valuable for the modelling and characterization of WASP-43 b, and can be explained alongside existing *Spitzer* data. Results of the same data set had been previously published in Gillon et al. (2012). We therefore used this data set as a benchmark to compare two different fitting methods and found out that the derived occultation depths agree within $\sim 2\sigma$.

We use both the *TESS* and HAWK-I data to place more detailed constraints on the atmospheres of two end-member hot Jupiters: WASP-43 b and WASP-18 b. To do this, we calculate self-consistent atmospheric models for each of these planets which explain the *TESS*, HAWK-I, and *Spitzer* observations. As WASP-43 b and WASP-18 b represent opposite extremes in temperature, these data allow a comparative study of exoplanet atmospheres across the hot and ultra-hot Jupiter regimes.

For both WASP-43 b and WASP-18 b, we find that inefficient energy redistribution is required to explain the data, though more so for WASP-18 b. In particular, we find that 10 per cent day–night energy redistribution can explain the observations of WASP-43 b, and no dayside or day–night energy redistribution (i.e. instant re-radiation) can explain the WASP-18 b observations. This is consistent with the observed trend of lower energy redistribution efficiencies for highly irradiated hot Jupiters (Cowan & Agol 2011). Consistent

with previous works (e.g. Blecic et al. 2014; Stevenson et al. 2014; Sheppard et al. 2017; Arcangeli et al. 2018), we find that a non-inverted (inverted) temperature profile is required to explain the thermal emission spectrum of WASP-43 b (WASP-18 b). We further find that thermal emission alone is able to explain the observations, without the need for reflected light resulting from clouds and/or hazes. Despite the extreme temperature contrast between WASP-43 b and WASP-18 b, the data analysed in this work therefore do not suggest the presence of clouds and/or hazes on the dayside of either planet.

As the population of hot Jupiters with *TESS* observations continues to grow, so too does our understanding of their atmospheric albedos. Furthermore, complementary infrared observations are essential in order to model and characterize these atmospheres in more detail. While optical occultation depths provide a measure of planetary geometric albedos, infrared spectra allow such albedos to be put into context, e.g. with atmospheric compositions and thermal profiles. Future more precise observations of albedos and thermal emission from hot Jupiters could enable population-level studies with joint constraints on the temperature structures, compositions, and sources of scattering in their atmospheres.

ACKNOWLEDGEMENTS

M. Blažek, P. Kabáth, and M. Skarka would like to acknowledge a MŠMT INTER-TRANSFER grant number LTT20015. A. Piette acknowledges financial support from the Science and Technology Facilities Council (STFC), UK, towards her doctoral programme. M. Skarka acknowledges the support from OP VVV Postdoc@MUNI (No. CZ.02.2.69/0.0/0.0/16_027/0008360). C. Cáceres acknowledges support by ANID BASAL project FB210003 and ICM Núcleo Milenio de Formación Planetaria, NPF. Based on observations collected at the European Southern Observatory under ESO programme 086.C-0222(B). This paper includes data collected by the *TESS* mission. Funding for the *TESS* mission is provided by the NASA's Science Mission Directorate. We acknowledge IRAF, distributed by the National Optical Astronomy Observatory, which is operated by the Association of Universities for Research in Astronomy (AURA) under a cooperative agreement with the National Science Foundation. We thank the editor and the anonymous reviewers for their helpful comments which improved quality of the article.

DATA AVAILABILITY

The data underlying this article are available from ESO archive via the query form (http://archive.eso.org/eso/eso_archive_main.html) under the programme specified in Acknowledgements. This article also includes data collected by the *TESS* mission, which are publicly available from the Mikulski Archive for Space Telescopes (MAST) (https://archive.stsci.edu/).

REFERENCES

Adams D., Kataria T., Batalha N., Gao P., Knutson H., 2022, ApJ, 926, 157
Anderson D. R. et al., 2010, A&A, 513, L3
Angerhausen D., DeLarme E., Morse J. A., 2015, PASP, 127, 1113
Arcangeli J. et al., 2018, ApJ, 855, L30
Arcangeli J. et al., 2019, A&A, 625, A136
Barber R. J., Strange J. K., Hill C., Polyansky O. L., Mellau G. C., Yurchenko S. N., Tennyson J., 2014, MNRAS, 437, 1828
Batalha N. M. et al., 2011, ApJ, 729, 27
Baxter C. et al., 2020, A&A, 639, A36
Beatty T. G. et al., 2020, AJ, 160, 211
Bell K. L., Berrington K. A., 1987, J. Phys. B Atomic Mol. Phys., 20, 801
Bell T. J. et al., 2017, ApJ, 847, L2
Blecic J. et al., 2014, ApJ, 781, 116
Borucki W. J. et al., 2010, Science, 327, 977
Bourrier V. et al., 2020, A&A, 637, A36
Brandeker A. et al., 2022, A&A, 659, L4
Burrows A., Sharp C. M., 1999, ApJ, 512, 843
Burrows A., Volobuyev M., 2003, ApJ, 583, 985
Burrows A., Budaj J., Hubeny I., 2008a, ApJ, 678, 1436
Burrows A., Ibgui L., Hubeny I., 2008b, ApJ, 682, 1277
Casali M. et al., 2006, in McLean I. S., Iye M., eds, Society of Photo-Optical Instrumentation Engineers (SPIE) Conference Series. SPIE, Bellingham, p. 62690W
Chakrabarty A., Sengupta S., 2019, AJ, 158, 39
Chen G. et al., 2014, A&A, 563, A40
Cowan N. B., Agol E., 2011, ApJ, 729, 54
Dai F., Winn J. N., Yu L., Albrecht S., 2017, AJ, 153, 40
Demory B.-O. et al., 2011, ApJ, 735, L12
Demory B.-O. et al., 2013, ApJ, 776, L25
Enoch B. et al., 2011, AJ, 142, 86
Esteves L. J., De Mooij E. J. W., Jayawardhana R., 2015, ApJ, 804, 150
Evans T. M. et al., 2013, ApJ, 772, L16
Fraine J. et al., 2021, AJ, 161, 269
Gandhi S., Madhusudhan N., 2017, MNRAS, 472, 2334
Gandhi S., Madhusudhan N., 2019, MNRAS, 485, 5817
Gandhi S., Madhusudhan N., Mandell A., 2020, AJ, 159, 232
Gibson N. P., 2014, MNRAS, 445, 3401
Gibson N. P. et al., 2010, MNRAS, 404, L114
Gibson N. P., Aigrain S., Roberts S., Evans T. M., Osborne M., Pont F., 2012, MNRAS, 419, 2683
Gibson N. P., Aigrain S., Barstow J. K., Evans T. M., Fletcher L. N., Irwin P. G. J., 2013a, MNRAS, 428, 3680
Gibson N. P., Aigrain S., Barstow J. K., Evans T. M., Fletcher L. N., Irwin P. G. J., 2013b, MNRAS, 436, 2974
Gillon M. et al., 2010, A&A, 511, A3
Gillon M. et al., 2011, A&A, 533, A88
Gillon M. et al., 2012, A&A, 542, A4
Gordon I. E. et al., 2017, J. Quant. Spec. Radiat. Transf., 203, 3
Günther M. N., Daylan T., 2019, Astrophysics Source Code Library, record ascl:1903.003
Günther M. N., Daylan T., 2021, ApJS, 254, 13
Harris G. J., Tennyson J., Kaminsky B. M., Pavlenko Y. V., Jones H. R. A., 2006, MNRAS, 367, 400
Harrison J. H. D., Bonsor A., Madhusudhan N., 2018, MNRAS, 479, 3814
Hellier C. et al., 2009, Nature, 460, 1098
Hellier C. et al., 2011, A&A, 535, L7
Heng K., Demory B.-O., 2013, ApJ, 777, 100
Heng K., Morris B. M., Kitzmann D., 2021, Nature Astron., 5, 1001
Hoyer S., Pallé E., Dragomir D., Murgas F., 2016, AJ, 151, 137
Huber K. F., Czesla S., Schmitt J. H. M. M., 2017, A&A, 597, A113
Husser T.-O., Wende-von Berg S., Dreizler S., Homeier D., Reiners A., Barman T., Hauschildt P. H., 2013, A&A, 553, A6
Jenkins J. M. et al., 2016, in Chiozzi G., Guzman J. C., eds, Proc. SPIE Conf. Ser. Vol. 9913, Software and Cyberinfrastructure for Astronomy IV. SPIE, Bellingham, p. 99133E
John T. L., 1988, A&A, 193, 189
Johnson J. A. et al., 2011, ApJ, 735, 24
Keating D., Cowan N. B., 2017, ApJ, 849, L5
Kipping D. M., Spiegel D. S., 2011, MNRAS, 417, L88
Kissler-Patig M. et al., 2008, A&A, 491, 941
Kreidberg L. et al., 2014, ApJ, 793, L27
Lothringer J. D., Barman T., Koskinen T., 2018, ApJ, 866, 27
Maciejewski G. et al., 2016, AcA, 66, 55
Madhusudhan N., 2019, ARA&A, 57, 617
Madhusudhan N., Agúndez M., Moses J. I., Hu Y., 2016, Space Sci. Rev., 205, 285

Mallonn M., Köhler J., Alexoudi X., von Essen C., Granzer T., Poppenhaeger K., Strassmeier K. G., 2019, A&A, 624, A62
Maxted P. F. L. et al., 2013, MNRAS, 428, 2645
McKemmish L. K., Yurchenko S. N., Tennyson J., 2016, MNRAS, 463, 771
McKemmish L. K., Masseron T., Hoeijmakers H. J., Perez-Mesa V., Grimm S. L., Yurchenko S. N., Tennyson J., 2019, MNRAS, 488, 2836
Moriarty J., Madhusudhan N., Fischer D., 2014, ApJ, 787, 81
Morley C. V., Fortney J. J., Kempton E. M. R., Marley M. S., Visscher C., Zahnle K., 2013, ApJ, 775, 33
Niraula P., Redfield S., de Wit J., Dai F., Mireles I., Serindag D., Shporer A., 2018, preprint (arXiv:1812.09227)
Parmentier V., Fortney J. J., Showman A. P., Morley C., Marley M. S., 2016, ApJ, 828, 22
Parmentier V. et al., 2018, A&A, 617, A110
Parviainen H., Aigrain S., 2015, MNRAS, 453, 3821
Piette A. A. A., Madhusudhan N., McKemmish L. K., Gandhi S., Masseron T., Welbanks L., 2020, MNRAS, 496, 3870
Pirard J.-F. et al., 2004, in Moorwood A. F. M., Iye M., eds, Proc. SPIE Conf. Ser. Vol. 5492, Ground-based Instrumentation for Astronomy. SPIE, Bellingham, p. 1763
Pollacco D. L. et al., 2006, PASP, 118, 1407
Richard C. et al., 2012, J. Quant. Spec. Radiat. Transf., 113, 1276
Ricker G. R. et al., 2015, J. Astron. Telesc. Instr. Syst., 1, 014003
Rothman L. S. et al., 2010, J. Quant. Spec. Radiat. Transf., 111, 2139
Rothman L. S. et al., 2013, J. Quant. Spec. Radiat. Transf., 130, 4
Saeed M. I., Goderya S. N., Chishtie F. A., 2022, New A, 91, 101680
Saha S., Chakrabarty A., Sengupta S., 2021, AJ, 162, 18
Sheppard K. B., Mandell A. M., Tamburo P., Gandhi S., Pinhas A., Madhusudhan N., Deming D., 2017, ApJ, 850, L32
Shporer A., Hu R., 2015, AJ, 150, 112
Shporer A. et al., 2019, AJ, 157, 178
Siebenmorgen R., Carraro G., Valenti E., Petr-Gotzens M., Brammer G., Garcia E., Casali M., 2011, Messenger, 144, 9
Smith J. C. et al., 2012a, PASP, 124, 1000
Smith A. M. S. et al., 2012b, AJ, 143, 81
Southworth J. et al., 2009, ApJ, 707, 167
Stevenson K. B. et al., 2014, Science, 346, 838
Stevenson K. B. et al., 2017, AJ, 153, 68
Stumpe M. C. et al., 2012, PASP, 124, 985
Tody D., 1986, in Crawford D. L., ed., Proc. SPIE Conf. Ser. Vol. 627. SPIE, Bellingham, p. 733
Tody D., 1993, in Hanisch R. J., Brissenden R. J. V., Barnes J., eds, ASP Conf. Ser. Vol. 52, Astronomical Data Analysis Software and Systems II. Astron. Soc. Pac., San Francisco, p. 173
Tregloan-Reed J., Southworth J., 2013, MNRAS, 431, 966
White W. B., Johnson S. M., Dantzig G. B., 1958, J. Chem. Phys., 28, 751
Winn J. N., 2010, Exoplanet Transits and Occultations. Univ. Arizona Space Science Series, University of Arizona Press, Tucson, AZ, p. 55
Wong I. et al., 2020a, AJ, 160, 88
Wong I. et al., 2020b, AJ, 160, 155
Yurchenko S. N., Tennyson J., 2014, MNRAS, 440, 1649
Yurchenko S. N., Barber R. J., Tennyson J., 2011, MNRAS, 413, 1828
Yurchenko S. N., Tennyson J., Barber R. J., Thiel W., 2013, J. Mol. Spectr., 291, 69
Zhou G., Bayliss D. D. R., Kedziora-Chudczer L., Tinney C. G., Bailey J., Salter G., Rodriguez J., 2015, MNRAS, 454, 3002

This paper has been typeset from a TEX/LATEX file prepared by the author.